

REPORTS

$^{13}\text{C}/^{12}\text{C}$ distribution and changed with Milankovich forcing. In addition, the existence of deglacial $\delta^{13}\text{C}$ minima in tropical surface water records (2, 3) has been difficult to explain because the nutrient increase implied by the $\delta^{13}\text{C}$ shift is not supported by evidence of increased upwelling in these presently nutrient-poor regions (2). Because the $\delta^{13}\text{C}$ of atmospheric CO_2 was lower at the onset of the deglaciation, tropical surface water $\delta^{13}\text{C}_{\text{DIC}}$ would have decreased via air-sea equilibration without an accompanying nutrient change. Such a mechanism is analogous to the invasion of low $\delta^{13}\text{C}$ anthropogenic CO_2 into the modern surface ocean (7). Taken as a whole, the timing and distribution of the deglacial carbon isotope minimum in tropical marine sediments is consistent with a Southern Ocean origin, with advection through intermediate waters and atmospheric equilibration providing the high-latitude-tropical connection.

References and Notes

1. N. J. Shackleton, M. A. Hall, J. Line, C. Shuxi, *Nature* **306**, 319 (1983).
2. D. W. Oppo, R. G. Fairbanks, *Paleoceanography* **4**, 333 (1989).
3. W. B. Curry, T. J. Crowley, *Paleoceanography* **2**, 489 (1987).
4. R. R. Schneider et al., in *Upwelling Systems: Evolution Since the Early Miocene*, C. P. Summerhayes, W. L. Prell, K. C. Ermeis, Eds. (Geological Society, London, 1992), pp. 285–297.
5. U. S. Ninnemann, C. D. Charles, *Paleoceanography* **12**, 560 (1997).
6. N. J. Shackleton, in *The Fate of Fossil Fuel CO_2 in the Oceans*, N. R. Andersen, A. Malahoff, Eds. (Plenum, New York, 1977), pp. 401–427.
7. J. Lynch-Stieglitz, R. G. Fairbanks, C. D. Charles, *Paleoceanography* **9**, 7 (1994).
8. B. D. Marino, M. B. McElroy, R. J. Salawitch, W. G. Spaulding, *Nature* **357**, 461 (1992).
9. H. J. Smith, H. Fischer, M. Wahnen, D. Mastroianni, B. Deck, *Nature* **400**, 248 (1999).
10. D. W. Lea, D. K. Pak, H. J. Spero, *Science* **289**, 1719 (2000).
11. M. Tsuchiya, R. Lukas, R. A. Fine, E. Firing, E. J. Lindstrom, *Prog. Oceanogr.* **23**, 101 (1989).
12. R. Lukas, *Prog. Oceanogr.* **16**, 63 (1986).
13. C. D. Charles, R. G. Fairbanks, *Nature* **355**, 416 (1992).
14. J. Toggweiler, D. Dixon, W. S. Broecker, *J. Geophys. Res.* **96**, 20467 (1991).
15. K. Hanawa, L. D. Talley, in *Ocean Circulation and Climate*, G. Siedler, J. Church, Eds. (Academic Press, San Diego, 2001), pp. 373–393.
16. C. D. Charles, R. G. Fairbanks, in *Geological History of the Polar Oceans: Arctic Versus Antarctic*, U. Bleil, J. Thiede, Eds. (Kluwer Academic, Dordrecht, Netherlands, 1990), pp. 519–538.
17. M. Tsuchiya, *Deep-Sea Res. I* **38**, S273 (1991).
18. F. J. Millero, W. Yao, K. Lee, J.-Z. Zhang, D. M. Campbell, *Deep-Sea Res. II* **45**, 1115 (1998).
19. R. G. Fairbanks, M. Sverdrup, R. Free, P. H. Wiebe, A. W. H. Bé, *Nature* **298**, 841 (1982).
20. J. R. Petit et al., *Nature* **399**, 429 (1999).
21. H. Gildor, E. Tziperman, *Paleoceanography* **15**, 605 (2000).
22. K. C. Taylor et al., *Nature* **366**, 549 (1993).
23. Accelerator mass spectrometry (AMS) ^{14}C ages were determined on two samples of monospecific *N. dutertrei* (10 to 12 mg; ~300 shells) at the Center for AMS, Lawrence Livermore National Laboratory. Radiocarbon ages were calibrated to calendar ages using the CALIB program (version 4.3) (<http://calib.org/calib/>) and a ΔR of 135 ± 40 . The two late glacial ages presented here are corrected for an apparent Galapagos surface water reservoir age of 635 years.
24. N. J. Shackleton et al., *Nature* **335**, 708 (1988).
25. Unpublished *N. dutertrei* $\delta^{13}\text{C}$ data from TR163-31B were provided by N. J. Shackleton.
26. T. Sowers et al., *Paleoceanography* **8**, 737 (1993).
27. D. W. Oppo, R. G. Fairbanks, *Earth Planet. Sci. Lett.* **86**, 1 (1987).
28. W. S. Broecker et al., *Radiocarbon* **32**, 119 (1990).
29. R. François et al., *Nature* **389**, 929 (1997).
30. J. R. Toggweiler, *Paleoceanography* **14**, 571 (1999).
31. D. M. Sigman, E. A. Boyle, *Nature* **407**, 859 (2000).
32. B. B. Stephens, R. F. Keeling, *Nature* **404**, 171 (2000).
33. M. A. Morales Maqueda, S. Rahmstorf, *Geophys. Res. Lett.* **29**, 10.1029/2001GL013240 (2002).
34. A. Mackensen, M. Rudolph, G. Kuhn, *Global Planet. Change* **30**, 197 (2001).
35. A. C. Mix, N. G. Pisias, W. R. Zahn, C. Lopez, K. Nelson, *Paleoceanography* **6**, 205 (1991).
36. B. E. Bernis, H. J. Spero, J. Bijma, D. W. Lea, *Paleoceanography* **13**, 150 (1998).
37. H. J. Spero et al., in preparation.
38. We thank J. Kennett for samples, J. Bijma, R. Zeebe, A. Wischmeyer, and B. Hoenisch for comments and suggestions, L. Talley for discussion on Pacific ocean circulation, T. Guilderson for AMS dates, E. Kalve and D. Pak for sample preparation, and L. Juranek and D. Winter for technical assistance. F. Miller kindly provided unpublished IRONEX cruise water column data. Supported by NSF grants OCE-9903632 (H.J.S.) and OCE-0117886 (D.W.L.) and a fellowship to H.J.S. from the Hanse Institute for Advanced Study.

27 December 2001; accepted 20 March 2002

Control of the Selectivity of the Aquaporin Water Channel Family by Global Orientational Tuning

**Emad Tajkhorshid,^{1*} Peter Nollert,^{2†} Morten Ø. Jensen,^{1‡}
Larry J. W. Miercke,² Joseph O'Connell,²
Robert M. Stroud,^{2§} Klaus Schulten^{1§}**

Aquaporins are transmembrane channels found in cell membranes of all life forms. We examine their apparently paradoxical property, facilitation of efficient permeation of water while excluding protons, which is of critical importance to preserving the electrochemical potential across the cell membrane. We have determined the structure of the *Escherichia coli* aquaglyceroporin GlpF with bound water, in native (2.7 angstroms) and in W48F/F200T mutant (2.1 angstroms) forms, and carried out 12-nanosecond molecular dynamics simulations that define the spatial and temporal probability distribution and orientation of a single file of seven to nine water molecules inside the channel. Two conserved asparagines force a central water molecule to serve strictly as a hydrogen bond donor to its neighboring water molecules. Assisted by the electrostatic potential generated by two half-membrane spanning loops, this dictates opposite orientations of water molecules in the two halves of the channel, and thus prevents the formation of a "proton wire," while permitting rapid water diffusion. Both simulations and observations revealed a more regular distribution of channel water and an increased water permeability for the W48F/F200T mutant.

Efficient permeation of water across cell membranes is mediated by a family of transmembrane water channels called aquaporins (AQP)

(1, 2). More than ten different genes encoding AQPs have been identified in the human genome, and their defective forms are known to cause diseases including nephrogenic diabetes insipidus, Sjögren's syndrome, and congenital cataract formation (3). They share the remarkable property of effective water conductance at rates close to 10^9 s^{-1} combined with a strict exclusion of all ions including protons (4). Aquaglyceroporins such as human AQP7, a glycerol specific channel in adipose tissue, and the *E. coli* glycerol channel, GlpF, belong to a subfamily that possesses the additional capability of passive and stereoselective carbohydrate transport (5). The recently determined structure of GlpF at 2.2 Å resolution with three bound glycerol molecules (6, 7) explains the channel's specificity and set the stage for molecular dynamics (MD) simulations to reveal the pathway

¹Theoretical Biophysics Group, Beckman Institute, University of Illinois at Urbana-Champaign, 405 North Mathews, Urbana, IL 61801, USA. ²Department of Biochemistry and Biophysics, School of Medicine, University of California at San Francisco, San Francisco, CA 94143, USA.

*These authors contributed equally to this work.
†Present address: Emerald BioStructures, Bainbridge Island, WA 98110, USA.

‡Visiting from Membrane and Statistical Physics Group, Department of Chemistry, Technical University of Denmark; present address: Quantum Protein Centre, Department of Physics, Technical University of Denmark, DK-2800 Lyngby, Denmark.

§To whom correspondence should be addressed. E-mail: stroud@msg.ucsf.edu (R.M.S.) or schulte@ks.uiuc.edu (K.S.).

and mechanism of conduction (8). The x-ray crystal structure of a related human AQP1 has also been reported recently (9).

The high proton mobility in bulk water is readily explained by the Grothuss mechanism involving proton tunneling from one water molecule to the next and rearrangement of hydrogen bonds (10). Proton conductance in proteins occurs through a "proton wire," in which a single-file arrangement of properly hydrogen-bonded

water molecules and polar groups of protein, provides an optimal pathway for efficient proton transfer (11–13), the latter requiring, however, a reorientation of water molecules. Implied by the single file of glycerol and water molecules in glycerol saturated GlpF (GlpF+G) (6, 8), the water conducting property of AQPs suggests that they support a column of water molecules inside the channel, raising the long standing question as to why protons are so effectively

blocked. In order to elucidate the origin of proton exclusion and the molecular mechanism of water diffusion in AQPs, we determined in the absence of glycerol the crystal structure of the native (GlpF-G) and the W48F/F200T mutant (GlpFW48F/F200T) forms of GlpF (Table 1) and carried out MD simulations (14) of membrane-embedded GlpF+G, GlpF-G, and GlpFW48F/F200T tetrameric channels to reveal diffusive behavior and positions and orienta-

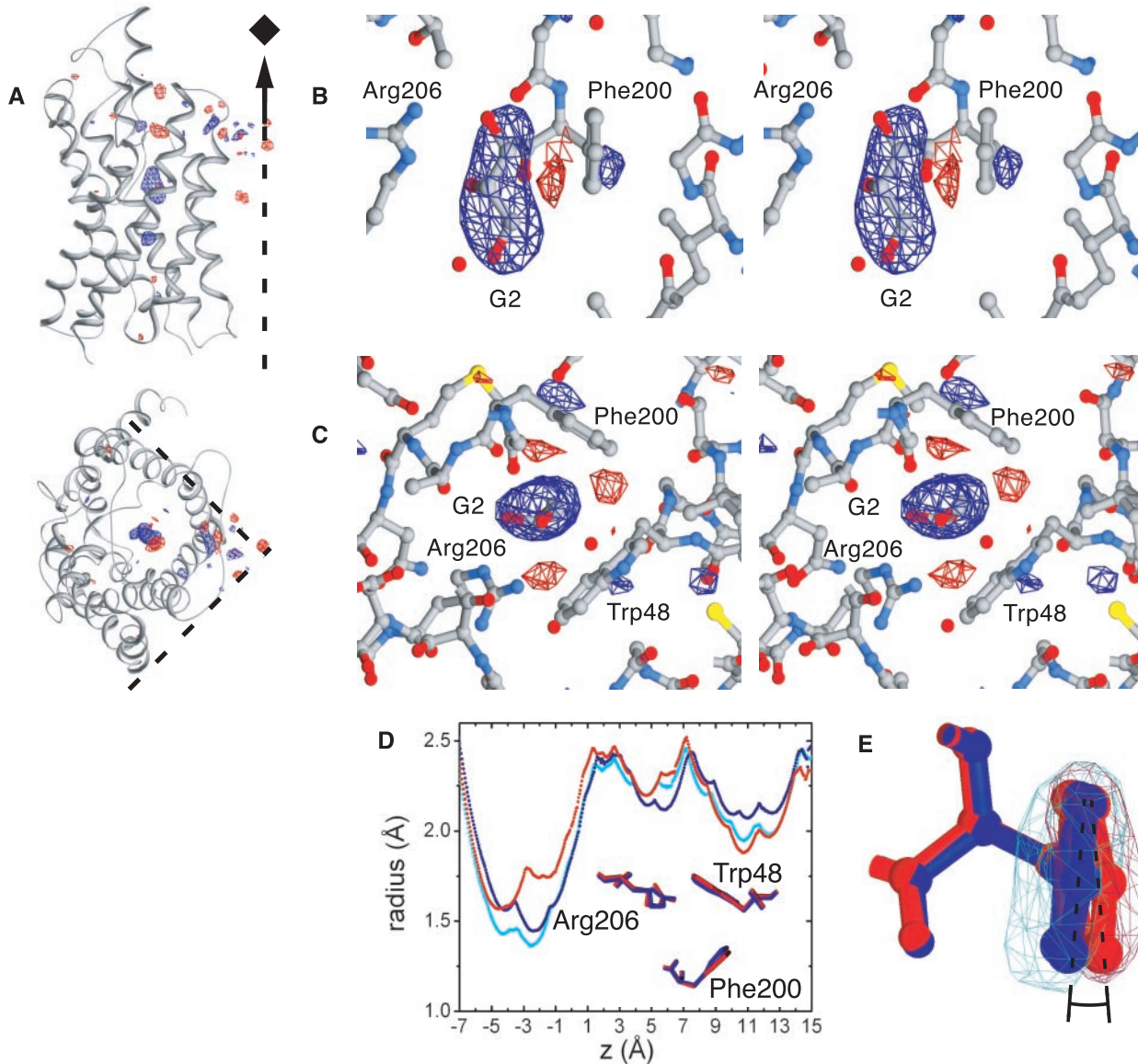


Fig. 1. Structural differences between the glycerol-bound form (GlpF+G) and the water bound form (GlpF-G) of the glycerol channel. **(A)** Model of monomeric GlpF with a superimposed $F_o(\text{water}) - F_c(\text{glycerol})$ Fourier difference map contoured at 2σ with positive (red), and negative density (blue). Views are perpendicular and along the fourfold symmetry axis. Considerable difference density is present inside the substrate conducting channel, along the fourfold symmetry axis, and in between. **(B)** Close up stereoimage of the selectivity filter region of GlpF+G with the superimposed Fourier difference map (contoured at 1.7σ). View as in (A). Glycerol 2 (G2) is encompassed by negative density, demonstrating its absence in (GlpF-G). The distribution of positive and negative difference density around Phe²⁰⁰ indicates a shift in its position. **(C)** Close up stereoimage as in (B) but with view along the channel axis. Positive difference density around Trp⁴⁸

and Phe²⁰⁰ toward the channel center and negative difference density on the opposite side indicate their shifted position in (GlpF+G). **(D)** Comparison of channel radii [(GlpF-G)_A, light blue; (GlpF-G)_B, dark blue; (GlpF+G), red; (see Table 1)] determined by the Hole2 program (28). In the absence of glycerol the constriction ($z = -4.5$) becomes narrower by about 10% and is shifted by about 2 Å ($z = -2.5$). (Inset) Superposition of the channel constraining residues in the selectivity filter of (GlpF+G), (red) and (GlpF-G)_B, (blue). **(E)** Rotation of Phe200 in GlpF+G (red) and (GlpF-G)_B (blue), viewed along its aromatic plane. The $2F_o - F_c$ electron density maps are contoured at 2σ . Although backbone atom positions remain unchanged, the phenyl ring in (GlpF-G)_A and (GlpF-G)_B is rotated clockwise relative to GlpF+G by 8.8° and 6.1°, respectively (corresponding to movements of 0.44 and 0.58 Å for $C_{\delta 1}$ and 0.61 and 0.74 Å for $C_{\epsilon 1}$).

tions of water molecules inside the channel.

The crystallographic structures of GlpF+G and GlpF-G are virtually identical (Table 1). The most pronounced structural changes, revealed by the $F_o(\text{water}) - F_c(\text{glycerol})$ difference map (Fig. 1), are small but significant in the orientation of the three selectivity filter (SF) lining residues, Trp⁴⁸, Phe²⁰⁰, and Arg²⁰⁶, and toward the center of the narrowest portion of the channel (Fig. 1, C through E). The observed subtle changes in the crystal structure are within the expected thermal fluctuations in MD simulations (at 310 K), yet a slightly increased fluctuation of Trp⁴⁸ in GlpF-G relative to GlpF+G is discernible from the simulations [see supplementary materials (15)]. Thus, in the water-

bound state, the channel diameter is narrower at its constriction by $\sim 0.4 \text{ \AA}$, indicating the intimate steric interaction between glycerol and channel at the SF region.

The analysis of the 4 ns MD trajectory of GlpF-G reveals a hydrogen-bonded single file of water molecules in the 20 \AA constriction region of the channel. The integrity of the single file is maintained throughout the simulation and water translocation along the channel axis is accordingly correlated [see supplementary materials (15)]. The simulations exhibit a one-dimensional water diffusion in the constriction region [see supplementary materials (15)], corresponding to a diffusion constant of $0.46 \times 10^{-5} \text{ cm}^2 \text{ s}^{-1}$, which compares well with the

observed value of 0.4×10^{-5} to $0.8 \times 10^{-5} \text{ cm}^2 \text{ s}^{-1}$ for AQP1 (16). Eighteen full water permeation events through the 20 \AA constriction region of the four channels were observed during the 4-ns MD simulation of GlpF-G. The conduction rate ($1.1 \text{ H}_2\text{O/ns/channel}$) compares satisfactorily with the experimentally deduced flux for GlpF (3, 17, 18), $0.5 \times 10^9 \text{ s}^{-1}$, and with the flux observed in MD simulations reported recently (19).

The observed electron density assigned to channel water corresponds closely to the distribution of water molecules determined by MD (Fig. 2). Water positions and orientations indicate that the molecules are all hydrogen donors to the line of carbonyl oxygen atoms that face

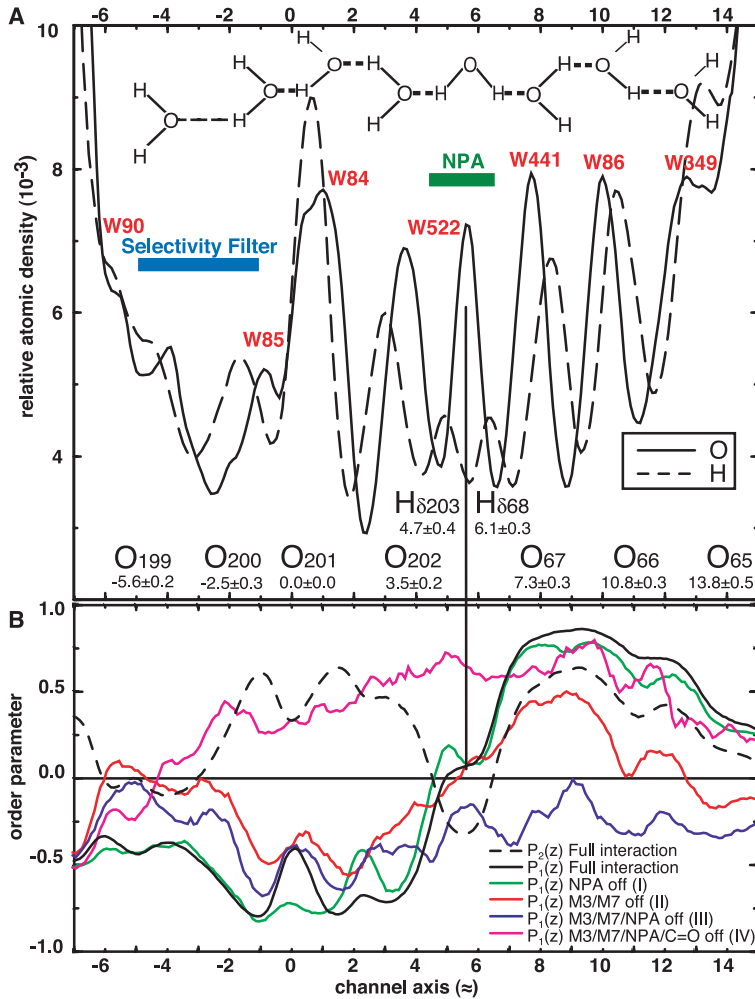
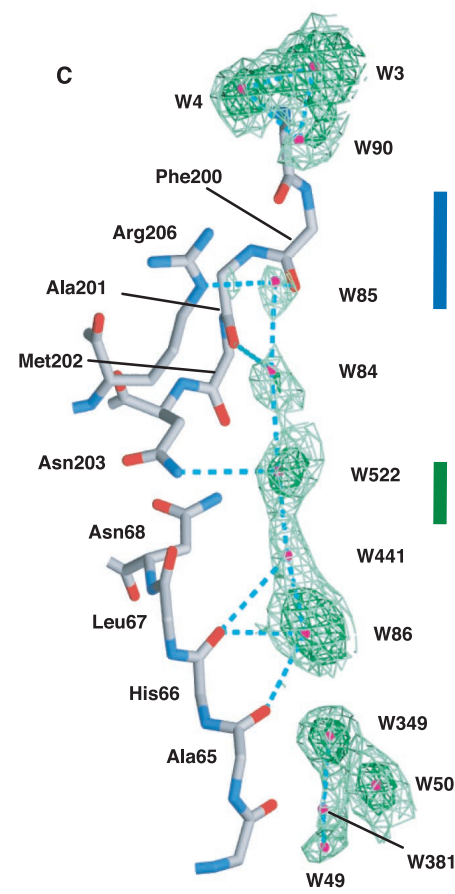


Fig. 2. (A) Simulated distributions of O and H atoms of water molecules inside the GlpF-G channel. The central peak in the O distribution at 5.4 \AA corresponds to the midpoint between the NPA motifs (vertical line). The systematic shift of the H peaks relative to the O peaks implies that the schematically illustrated water orientation is present in the channel, as confirmed in panel (B). The positions (Mean \pm SD) of hydrogen bonding sites in the channel closely correlate with water atomic distributions. The origin of the z-axis is Ala201:O. (B) Water orientation in GlpF-G depicted by order parameters $P_1(z) = \langle \cos\theta \rangle$ and $P_2(z) = 1/2(3\cos^2\theta - 1)$; θ is the angle between the membrane normal and the normalized (unit) water dipole vector; $P_2(z)$ differentiates between orthogonal ($P_2(z) = -0.5$) and isotropic average orientation ($P_2(z) = 0$). Black lines represent the order parameters calculated in the presence of



the full electric field of the channel; colored lines are $P_1(z)$ calculated after turning off the charges on the NH_2 groups of the NPA asparagines (I), turning off the charges on the backbone atoms of the two half-membrane spanning helices M3 and M7 (II), combining I and II (III), and combining I and II and turning off charges on the channel lining carbonyl groups (IV). (C) Observed location of water molecules in the water bound channel (GlpF-G_A) with an overlaid $2F_o - F_c$ electron density map contoured at 1.5σ (light green) and 2σ (dark green). Positions of the water molecules were determined iteratively from peaks in $F_o - F_c$ maps, starting from both, an empty channel and a water filled channel (and cross-checked by the corresponding omit maps). Hydrogen bonds are shown by blue dashed lines. An occupancy of 1 for all water positions was maintained in the subsequent refinement cycles.

the inside of the channel (8), with the exception of the central water molecule. The smeared out probability for locating these atoms within $-6 \text{ \AA} \leq z \leq 14 \text{ \AA}$, i.e., the constriction region, suggests water mobility. Alternating O and H peaks indicate hydrogen bonds between the water molecules. Gaps in the electron density are notable between W90 and W85 (5.5 Å apart), and W86 and W349 (4.5 Å apart). Furthermore, the electron density at the narrowest point of the channel at $z \approx -3 \text{ \AA}$, opposing the hydrogen donor NH_2 of the guanidino group of Arg^{206} , is low (Fig. 2C). These observations may be accounted for by the disorder of water molecules at these sites. Alternatively, there may be no water at all since the diffraction experiments were carried out at 100 K where translational and rotational motions of the water molecules freeze out (20, 21) and water transport in the channel does not occur (22). These sites lie close to the transition state in the conduction pathway (6), and might exhibit a small population at 100 K. The SF region shows a reduced water probability also in the 310 K MD simulations and an extrapolation to 100 K correlates closely with the observed low occupancy in this region.

Our MD simulations clearly show that start-

ing from the NPA center, water molecules are oriented in opposite directions in the two halves of the channel, with their hydrogen atoms pointing toward the exits (Figs. 2 and 3) as postulated by Murata *et al.* (23). An almost orthogonal orientation of water relative to the membrane normal is featured at $z \approx 5.4 \text{ \AA}$, the midpoint of the NPA motifs (Fig. 2A).

This arrangement contrasts with the uniform orientation of water molecules in gramicidin A, a water and a proton channel (13). Between the two NPA motifs, the central water oxygen atom becomes hydrogen bonded to the NH_2 s of Asn^{68} and Asn^{203} with the water dipole consequently restrained to lie perpendicular to the channel axis. Opposite the NPA motifs across the channel there are only hydrophobic residues, Ile^{187} , its flanking Val^{152} , and Leu^{159} , serving to prohibit a different hydrogen bonding pattern. Hence, the highly conserved and constrained Asn residues in an otherwise hydrophobic environment function to specifically hydrogen bond to a single water molecule, making its lone electron pairs unavailable as proton acceptors for the neighboring water molecules. As a result of the water orientation at the NPA center, the orientations of the neighboring water molecules

are constrained such that successive O-H bonds are oriented away from this central water, with the other O-H of each water hydrogen bonding to successive carbonyls in the channel lining. Thus, this bipolar orientation is propagated outward along the water file.

In addition to the hydrogen bond donors of the central asparagines, the α -helices M3 and M7 generate electrostatic fields directed toward the center of the channel (23) (Fig. 3), which stabilize the water configuration shown in Figs. 2 and 3. To test the relative contributions of the Asn NH_2 groups, the helix dipoles (9), and the line of carbonyls to the orientation of water molecules in the channel, four additional simulations, 0.5 ns each, were carried out in which one, two, or all of these effects were “turned off” (Fig. 2B). When the charges of the NH_2 -groups of the Asn^{68} and Asn^{203} side chains are turned off (I) the water configuration is partially affected. As the charges of the backbone atoms of the half-helices M3 and M7 are turned off (II), and as this is combined with I (III), the bipolar orientation of the single-file arrangement breaks down leading to a uniform water orientation in the channel, a potential proton wire. Although the dipoles of the channel lining

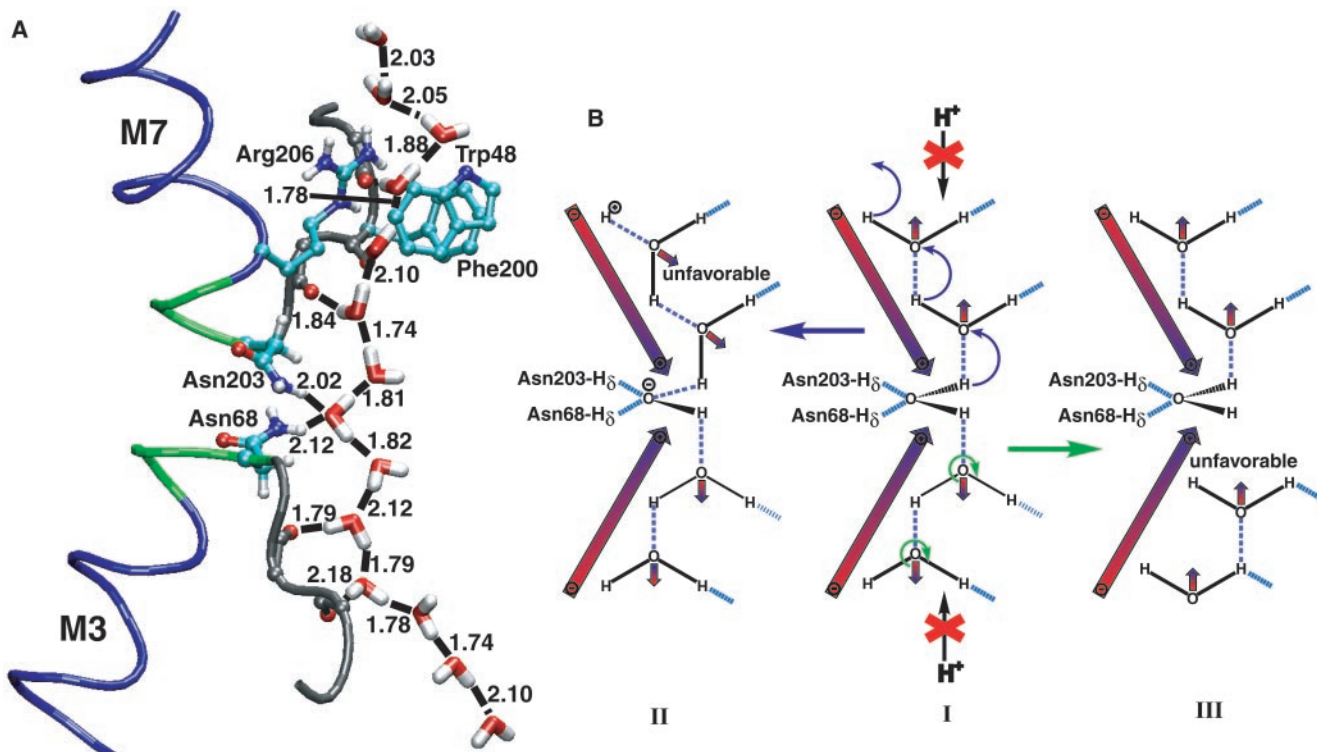


Fig. 3. (A) Snapshot from MD simulation revealing the orientation of the non-hydrogen bonded water network that precludes proton conduction in GlpF. The opposite orientations of water molecules in the two halves of the channel start from the central water molecule opposite the NPA motifs (residues 68–70 and 203–205 shown in green with the side chains of Asn^{68} and Asn^{203} displayed in licorice representation), and are stabilized by the electrostatic fields generated by the M3 and M7 helices (shown in blue), and by hydrogen bonds to the carbonyl groups in the non-helical parts of two half-membrane spanning repeats (shown in gray). The exposed carbonyl oxygens of residues 65–66 and 198–200 are displayed as red spheres. Residues Arg^{206} , Phe^{200} , and Trp^{48} constituting the selectivity filter appear in

light blue. (B) Schematic illustration of the proton preclusion. Initial protonation at any of the two termini of the single file (shown by black arrows in I) cannot be accomplished due to the adopted configuration. Proton release at any terminus can only propagate to the central water (blue curved arrows) and results in an unfavorable water orientation relative to the helical dipolar field as depicted in II; furthermore, a proton cannot be taken up by the other terminus to complete the transfer. Water reorientation (green arrows) leading to the availability of water oxygen atoms for outside protons at one terminus results in an unfavorable water orientation (III) and breaks the hydrogen bond network in the middle of the channel. Panel (A) was created with the molecular graphics program VMD (29).

carbonyl groups alone cannot maintain the bipolar orientation of water molecules, their absence (IV in Fig. 2B) significantly accelerates the relaxation toward orientational disorder. Therefore, these interactions combined establish a global orientation control mechanism that abrogates any proton transport through the channel.

The observed low occupancy of water molecules in the SF region of GlpF-G demonstrated by measurements and simulations (Fig. 2) may be the cause for the low rate of water permeation in GlpF. In order to assess such effects, a double mutant, GlpF^{W48F/F200T}, in which both the size and polarity of the channel were increased in the SF region, was studied by means of experimental measurements and MD simulations. Light scattering assays (18) on reconstituted vesicles indicated an increased water

permeation for GlpF^{W48F/F200T} over the wild-type GlpF [rate_{GlpF(W48F/F200T)}/rate_{wt-GlpF} = 1.25 ± 0.095 ; $n = 3$]. In close agreement with the observations, our MD simulations revealed a 38% increase in the number of permeated water molecules in GlpF^{W48F/F200T} (25 water molecules passed the constriction regions of the four channels in 4 ns).

As illustrated in Fig. 4A, both simulations and electron density data for GlpF^{W48F/F200T} indicate a significant increase of water density at the SF region (the mutation site), as compared to native GlpF (Fig. 2). Several water molecules are present in the electron density map of the SF region. The calculated density of water is now higher in this region than in the other parts of the channel (Fig. 4A). Otherwise, the position and orientation of water molecules in the constriction region of the channel do not show any

significant variation from those in GlpF-G (Fig. 2). In particular, the bipolar orientation of water molecules inside the channel is preserved after the mutations (Fig. 4B). We therefore predict that GlpF^{W48F/F200T} is also impermeable to protons, a prediction which is at variance with the SF-based mechanism for proton exclusion suggested in (19), but in line with observations that mutated *E. coli* cells grew without change in phenotype.

Proton transport along water chains requires a uniform orientation of hydrogen-bonded water molecules that permits reorientation during proton transfer, requirements neither of which is met by the bipolar water file in GlpF (Figs. 2 and 4). The faithful description of the GlpF^{W48F/F200T} mutant by our simulations gives credence to the suggested mechanism. In light of the absolute conservation of the NPA motifs and the conservation of structure throughout the AQPs (3, 6, 9), we propose that this mechanism of precluding proton conduction applies to the entire AQP family.

References and Notes

1. G. M. Preston, P. Piazza-Carroll, W. B. Guggino, P. Agre, *Science* **256**, 385 (1992).
2. P. Agre, M. Bonhivers, M. J. Borgnia, *J. Biol. Chem.* **273**, 14659 (1998).
3. M. Borgnia, S. Nielsen, A. Engel, P. Agre, *Annu. Rev. Biochem.* **68**, 425 (1999).
4. M. Zeidel et al., *Biochemistry* **33**, 1606 (1992).
5. K. B. Heller, E. C. Lin, T. H. Wilson, *J. Bacteriol.* **144**, 274 (1980).
6. D. Fu et al., *Science* **290**, 481 (2000).
7. P. Nollert, W. E. C. Harris, D. Fu, L. J. W. Miercke, R. M. Stroud, *FEBS Lett.* **504**, 112 (2001).
8. M. Ø. Jensen, E. Tajkhorshid, K. Schulten, *Structure* **9**, 1083 (2001).
9. H. Sui, B. Han, J. K. Lee, P. Walian, B. K. Jap, *Nature* **414**, 872 (2001).
10. C. J. T. de Grotthuss, *Ann. Chim.* **LVIII**, 54 (1806).
11. J. F. Nagle, H. J. Morowitz, *Proc. Natl. Acad. Sci. U.S.A.* **75**, 298 (1978).
12. Z. Schulten, K. Schulten, *Methods Enzymol.* **127**, 419 (1986).
13. R. Pomes, B. Roux, *Biophys. J.* **71**, 19 (1996).
14. GlpF was simulated in its tetrameric form (generated using the crystal structure [PDB entry 1FX8] (6)), embedded in a fully hydrated bilayer membrane, as described in more detail elsewhere (8). All glycerols (three per channel) were removed and replaced by six water molecules per channel; the number and positions of water molecules being suggested by the program DOWSER; the two crystallographically observed water molecules in each channel were kept. The total size of the simulated system of the wild-type GlpF in an elementary cell was 106,189 atoms, including the protein tetramer (15,356 atoms), 317 POPE (palmitoyl-oleoyl-phosphatidyl-ethanolamine) lipid molecules (39,625 atoms), 17,068 water molecules (51,204 atoms), and four chloride ions to neutralize the total charge. All titratable amino acids were modeled in their charged forms. Constant temperature (310 K) and pressure (1 atm), and periodic boundary conditions were assumed. The simulations were performed with the MD program NAMD (24) using the CHARMM27 force field with its improved parameters for lipids (25) and the TIP3P model for water (26). Coulomb forces were evaluated without cut-off using the Particle-Mesh-Ewald method. The system was simulated for 5 ns with an integration time step of 1 fs without geometrical restraints; 1 ns was consumed for equilibration, 4 ns for analysis. The wild-type system was also used in four additional simulations (I to IV) each lasting 500 ps in which various electrostatic forces were switched off in order to verify how the protein tunes the ordering of its channel water. For the simulations of

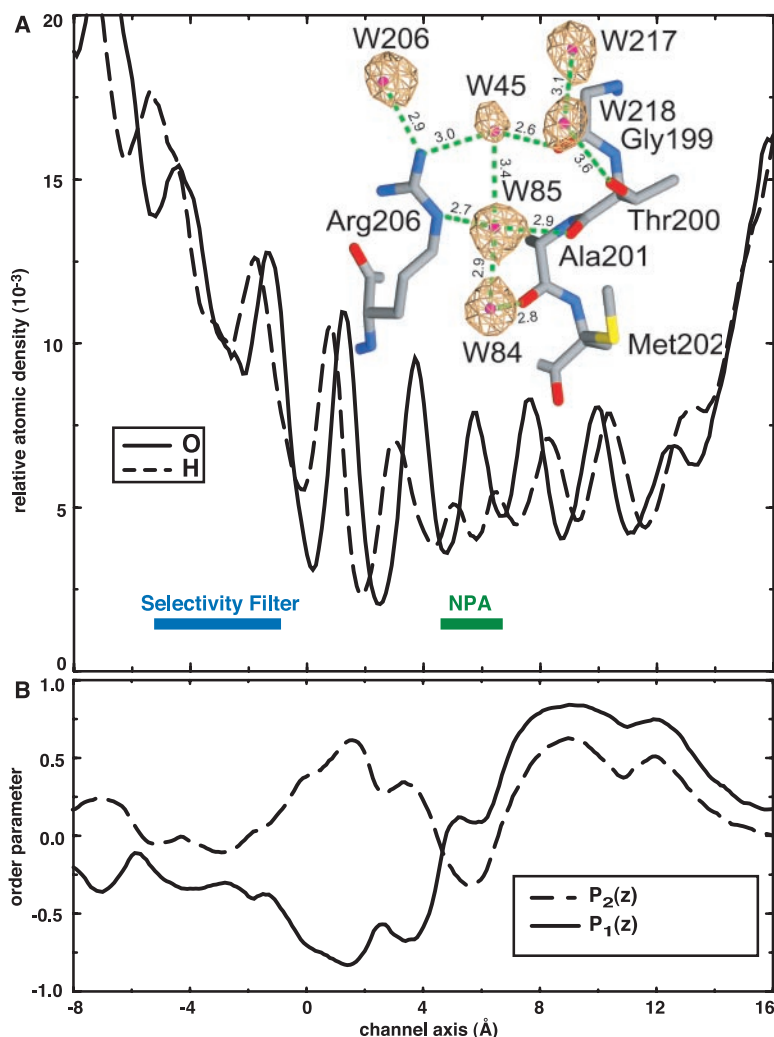


Fig. 4. Water distribution and orientation in GlpF^{W48F/F200T}. (A) Simulated distributions of O and H atoms of water in the constriction region of the channel ($-6 \text{ \AA} \leq z \leq 14 \text{ \AA}$). (Inset) Water molecules at the selectivity filter region of GlpF double mutant W48F/F200T with the superimposed $2F_s - F_c$ map, contoured at 1σ around selected water positions. Four novel water molecules W45, W206, W217, W218 form a hydrogen bond network with channel atoms and with each other. (B) Bipolar water orientation in the two halves of the channel, orthogonal orientation of the central water molecule, and isotropic distribution of water molecules outside the channel are illustrated by the calculated order parameters $P_1(z)$ and $P_2(z)$ (as described in Fig. 2).

REPORTS

Table 1. Crystallographic statistics. GlpF was overexpressed, purified, and crystallized as described (6), replacing glycerol by xylose (15% w/w) for (GlpF-G)_A and (GlpF-G)_B, a nontransported substrate (6). Single crystals were subject to x-ray diffraction at ALS beam line 5.0.2 using a CCD detector (Quantum IV). The crystals were in space group I422 and were isomorphous to crystals previously grown in 15% (w/w) glycerol. The structures were determined by direct isomorphous replacement using the protein component of 1FX8 and refined with CNS (27). The RMSD between 1FX8 (at 2.2 Å resolution) and (GlpF-G)_A is 0.26 Å, and (GlpF-G)_B is 0.51 Å and GlpF^{W48F/F200T} is 0.20 Å, the RMSD between (GlpF-G)_A and (GlpF-G)_B is 0.18 Å.

Crystal	(GlpF-G) _A	(GlpF-G) _B	GlpF ^{W48F/F200T}
Wavelength (Å)	1.1	1.1	1.0
Resolution (Å)	30–2.7	30–2.8	35–2.1
Observations	64951	51474	128187
Unique	10918	8698	25710
Unit cell size (a, c in Å)	96.05, 184.20	96.23, 184.37	96.93, 185.43
Completeness (%)	87.5	78.6	97.9
R _{merge} (%)	8.1	9.0	8.5
$\langle I/\sigma I \rangle$	14.0	16.9	16.0
<i>Refinement statistics</i>			
Number of reflections	9774/1144	7769/929	25674/1240
Number of nonhydrogen atoms	1997	1997	1994
Unobserved residues	1–5, 260–281	1–5, 260–281	1–5, 260–281
Resolution (Å)	30–2.7	30–2.8	35–2.1
R _{cryst} /R _{free} (%)	22.9/26.1	20.8/24.9	23.0/24.3
Average B factor (Å ²)	54.4	49.6	40.3
<i>Model geometry</i>			
Bond length deviation (Å)	0.007	0.009	0.0063
Bond angle deviation (°)	1.26	1.11	1.17

$\langle I/\sigma I \rangle$, mean signal-to-noise, where I is the integrated intensity of a measured reflection and σI is the estimated error in the measurement; $R_{\text{merge}} = \sum_{\text{hkl}} \sum_i |I_i(\text{hkl}) - \langle I_i(\text{hkl}) \rangle| / \sum_{\text{hkl}} \sum_i I_i(\text{hkl})$.

W48F/F200T double mutant, we started from the equilibrated model of the native protein in the membrane. After mutating the amino acids, the system was equili-

brated (1 ns), followed by a 4 ns simulation used in our analysis. Simulation conditions were the same as for wild-type GlpF.

DNA Repair Pathway Stimulated by the Forkhead Transcription Factor FOXO3a Through the Gadd45 Protein

Hien Tran,^{1*} Anne Brunet,^{1*} Jill M. Grenier,² Sandeep R. Datta,¹ Albert J. Fornace Jr.,³ Peter S. DiStefano,² Lillian W. Chiang,² Michael E. Greenberg^{1†}

The signaling pathway from phosphoinositide 3-kinase to the protein kinase Akt controls organismal life-span in invertebrates and cell survival and proliferation in mammals by inhibiting the activity of members of the FOXO family of transcription factors. We show that mammalian FOXO3a also functions at the G₂ to M checkpoint in the cell cycle and triggers the repair of damaged DNA. By gene array analysis, FOXO3a was found to modulate the expression of several genes that regulate the cellular response to stress at the G₂-M checkpoint. The growth arrest and DNA damage response gene *Gadd45a* appeared to be a direct target of FOXO3a that mediates part of FOXO3a's effects on DNA repair. These findings indicate that in mammals FOXO3a regulates the resistance of cells to stress by inducing DNA repair and thereby may also affect organismal life-span.

The binding of growth factors to specific receptor tyrosine kinases activates the phosphoinositide 3-kinase (PI3K) and the serine-threonine kinase Akt (also called

protein kinase B or PKB). Akt promotes cell survival and proliferation in part by directly phosphorylating and inhibiting members of the FOXO subfamily of fork-

- Supplementary materials are available at www.sciencemag.org/cgi/content/full/296/5567/525/DC1.
- J. B. Heymann, A. Engel, *News Physiol. Sci.* **14**, 187 (1999).
- M. J. Borgnia, D. Kozono, G. Calamita, P. C. Maloney, P. Agre, *J. Mol. Biol.* **291**, 1169 (1999).
- M. J. Borgnia, P. Agre, *Proc. Natl. Acad. Sci. U.S.A.* **98**, 2888 (2001).
- B. L. de Groot, H. Grubmüller, *Science* **294**, 2353 (2001).
- I. V. Kurinov, R. W. Harrison, *Acta Crystallogr. D* **51**, 98 (1995).
- D. Vitkup, D. Ringe, G. A. Petsko, M. Karplus, *Nature Struct. Biol.* **7**, 34 (2000).
- J. P. Cowin, A. A. Tsekouras, M. J. Ledema, K. Wu, G. B. Ellison, *Nature* **398**, 405 (1999).
- K. Murata et al., *Nature* **407**, 599 (2000).
- L. Kale et al., *J. Comput. Phys.* **151**, 283 (1999).
- A. D. MacKerell Jr. et al., *J. Phys. Chem. B* **102**, 3586 (1998).
- W. L. Jorgensen, J. Chandrasekhar, J. D. Madura, R. W. Impey, M. L. Klein, *J. Chem. Phys.* **79**, 926 (1983).
- A. Brünger et al., CNS program (1996).
- O. Smart, Hole2 program (<http://bach.bip.bham.ac.uk/osmart/hole/>).
- W. Humphrey, A. Dalke, K. Schulter, *J. Mol. Graph.* **14**, 33 (1996).
- Supported by NIH, and computer time provided by NRAC. E.T. and P.N. received postdoctoral support from the Human Frontier Science Program Organization. M.O.J. acknowledges financial support from The Danish Natural Science Research Council. We thank E. Hur and W. Harries for constructing mutants, and T. Earnest for help and support at the Advanced Light Source (ALS), Lawrence Berkeley National Laboratory. Coordinates of the structures have been deposited in the Research Collaboratory for Structural Bioinformatics (RCSB) Protein Data Bank [accession codes 1LDI, 1LDA, and 1LDF for (GlpF-G)_A, (GlpF-G)_B, and GlpF^{W48F/F200T}, respectively].

6 November 2001; accepted 14 March 2002

head transcription factors (1–3). In the nematode *Caenorhabditis elegans*, null mutants of the PI3K-Akt pathway lead to the activation of the worm FOXO transcription factor DAF-16, resulting in either an extension of adult life-span or, during development, an entrance into the long-lived larval stage termed dauer (4, 5). In both cases, the PI3K-Akt pathway mutants develop a resistance to stress that may account for the longevity phenotype observed (4, 6). One possibility is that in the mutant background, the activation of FOXO transcription factors may mediate the resistance to stress because DAF-16's activity is required for the transcriptional up-regulation of cytosolic catalase and superoxide dismutase, scavenger proteins that protect against oxidative damage (7, 8). In mammals, the role of the forkhead transcription

¹Division of Neuroscience, Children's Hospital and Department of Neurobiology, Harvard Medical School, Boston, MA 02115, USA. ²Millennium Pharmaceuticals, Inc., 640 Memorial Drive, Cambridge, MA 02139, USA. ³Building 37, Room 6144, NCI, National Institutes of Health, 37 Convent Drive MSC 4255, Bethesda, MD 20892, USA.

*These authors contributed equally to this work.

†To whom correspondence should be addressed. E-mail: michael.greenberg@tch.harvard.edu